

Effective Model for Massless Dirac Electrons on a Surface of Weak Topological Insulators

Takashi Arita and Yositake Takane*

*Department of Quantum Matter, Graduate School of Advanced Sciences of Matter,
Hiroshima University, Higashihiroshima, Hiroshima 739-8530, Japan*

(Received)

In a typical situation, gapless surface states of a three-dimensional (3D) weak topological insulator (WTI) appear only on the sides, leaving the top and bottom surfaces gapped. To describe massless Dirac electrons emergent on such side surfaces of a WTI, a two-dimensional (2D) model consisting of a series of one-dimensional helical channels is usually employed. However, an explicit derivation of such a model from a 3D bulk Hamiltonian has been lacking. Here, we explicitly derive an effective 2D model for the WTI surface states starting from the Wilson-Dirac Hamiltonian for the bulk WTI and establish a firm basis for the hitherto hypothesized 2D model. We show that the resulting 2D model accurately reproduces the excitation spectrum of surface Dirac electrons determined by the 3D model. We also show that the 2D model is applicable to a side surface with atomic steps.

1. Introduction

Three-dimensional (3D) weak topological insulators (WTIs) are known to be equivalent to stacked layers of two-dimensional (2D) quantum spin-Hall (QSH) insulators.^{1–3)} The stacking direction is specified by the weak vector $\boldsymbol{\nu} \equiv (\nu_1, \nu_2, \nu_3)$, where ν_1 , ν_2 , and ν_3 are called weak indices. Reflecting the feature of a 2D QSH insulator that it is gapped in its bulk but possesses a gapless one-dimensional (1D) helical channel at its edge,^{4,5)} a WTI accommodates low-energy electron states arising from helical edge channels only on its side surface. This should be contrasted to the case of strong topological insulators, in which low-energy electron states appear on every surface. We refer to low-energy surface electrons as Dirac electrons since they obey the massless Dirac equation. A characteristic feature of WTIs is that their low-energy surface states typically consist of two Dirac cones in the reciprocal space, in contrast to the case of strong topological insulators, where typically only one Dirac cone is present. Owing to this, the surface state of a WTI was considered to be weak against disorder, becoming gapped by scattering between two Dirac cones. However, it has been shown that a WTI is not necessarily weak.^{6–16)} As low-energy electron states on the side surface of a WTI are formed by a series of helical edge channels, they are significantly affected by whether the number of QSH layers stacked along $\boldsymbol{\nu}$ is even or odd.^{8, 11, 12)} If it is even, the helical edge channels acquire a finite-size gap owing to their mutual coupling. Contrastingly, if it is odd, one helical channel survives and the system has a gapless excitation spectrum. This parity dependence is another characteristic feature of surface Dirac electrons. Several materials have been proposed as possible

WTIs.^{17–20)}

To theoretically describe Dirac electrons on a side surface of WTIs, an effective 2D model consisting of coupled 1D helical channels has been proposed in Refs. 14 and 15. This model has two Dirac cones in the reciprocal space and is capable of describing the even-odd parity dependence of an excitation spectrum with respect to the number of QSH layers constituting a sample. However, the connection between such an effective 2D model for surface states and a 3D model for bulk WTIs has not been established concretely.

In this paper, we derive an effective 2D Hamiltonian for Dirac electrons on a side surface of WTIs starting from the 3D Wilson-Dirac Hamiltonian for bulk topological insulators. We show that the resulting 2D model is indeed equivalent to coupled 1D helical channels and that all parameters in it are determined by those of the original 3D model. By comparing the excitation spectrum of surface Dirac electrons obtained from the 2D model with that obtained from the 3D model, we confirm the validity of the effective model. We also show that the effective model is applicable to a side surface of WTIs with atomic steps. We set $\hbar = 1$ throughout this paper.

2. Derivation of the 2D Model

We start from the following Wilson-Dirac Hamiltonian for 3D topological insulators in the continuum limit:²¹⁾

$$H = \epsilon_{\mathbf{k}} \mathbf{1} + \begin{bmatrix} M_{\mathbf{k}} & Bk_z a & 0 & Ak_- a \\ Bk_z a & -M_{\mathbf{k}} & Ak_- a & 0 \\ 0 & Ak_+ a & M_{\mathbf{k}} & -Bk_z a \\ Ak_+ a & 0 & -Bk_z a & -M_{\mathbf{k}} \end{bmatrix}, \quad (1)$$

*takane@hiroshima-u.ac.jp

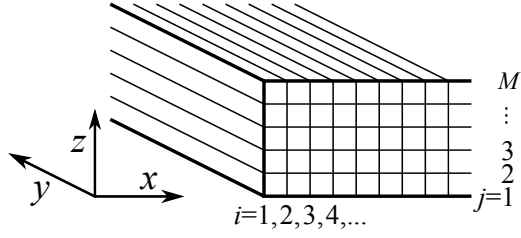


Fig. 1. Structure of a WTI sample considered in the text; it consists of M layers in the z -direction with $M \geq j \geq 1$ and is semi-infinite in the x -direction with $i \geq 1$, while it is infinitely long in the y -direction.

where $\mathbf{1}$ is the 4×4 unit matrix, a is the lattice constant, $k_{\pm} = k_x \pm ik_y$, and

$$\epsilon_{\mathbf{k}} = c_0 + c_{2\parallel}(k_x^2 + k_y^2)a^2 + c_{2\perp}k_z^2a^2, \quad (2)$$

$$M_{\mathbf{k}} = m_0 + m_{2\parallel}(k_x^2 + k_y^2)a^2 + m_{2\perp}k_z^2a^2. \quad (3)$$

The basis set $\{|\mathbf{k}\rangle_{1\uparrow}, |\mathbf{k}\rangle_{2\uparrow}, |\mathbf{k}\rangle_{1\downarrow}, |\mathbf{k}\rangle_{2\downarrow}\}$ is adopted in expressing H in the matrix form, where \uparrow, \downarrow and $1, 2$ respectively represent the spin and orbital degrees of freedom.

Among several topological phases described by this model in a discretized version,¹¹⁾ we choose the weak topological phase with $\boldsymbol{\nu} \equiv (0, 0, 1)$ as a typical example. In this phase, the system is equivalent to 2D QSH insulators stacked in the z -direction. We discretize the z - and x -coordinates and implement H on the square lattice on the xz -plane leaving the y -coordinate unchanged. The discretization of the z -coordinate is indispensable to take account of the parity effect that depends on whether the number of QSH layers is even or odd. Let us use the indices i and j respectively to specify lattice sites in the x - and z -directions. We assume that the system consists of M layers in the z -direction with $M \geq j \geq 1$ and is semi-infinite in the x -direction with $i \geq 1$ (see Fig. 1). We also assume that the system is infinitely long in the y -direction, so k_y remains a good quantum number. Our attention is focused on Dirac electrons emerging on the side surface of height M in the yz -plane. Let us introduce the four-component state vector for the (i, j) th site,

$$|i, j\rangle = [|i, j\rangle_{1\uparrow}, |i, j\rangle_{2\uparrow}, |i, j\rangle_{1\downarrow}, |i, j\rangle_{2\downarrow}]. \quad (4)$$

In terms of this vector, the discretized version of the Wilson-Dirac Hamiltonian is expressed as

$$H_{3D} = H_x + H_y + H_z \quad (5)$$

with

$$H_x = \sum_{i=1}^{\infty} \sum_{j=1}^M \left[|i, j\rangle h_0 \langle i, j| + \{ |i+1, j\rangle h_x^+ \langle i, j| + \text{h.c.} \} \right], \quad (6)$$

$$H_y = \sum_{i=1}^{\infty} \sum_{j=1}^M |i, j\rangle h_y \langle i, j|, \quad (7)$$

$$H_z = \sum_{i=1}^{\infty} \sum_{j=1}^{M-1} \{ |i, j+1\rangle h_z^+ \langle i, j| + \text{h.c.} \}. \quad (8)$$

Here, the 4×4 matrices are given by

$$h_0 = \tilde{c}_0 \mathbf{1} + \begin{bmatrix} \tilde{m}_0 & 0 & 0 & 0 \\ 0 & -\tilde{m}_0 & 0 & 0 \\ 0 & 0 & \tilde{m}_0 & 0 \\ 0 & 0 & 0 & -\tilde{m}_0 \end{bmatrix}, \quad (9)$$

$$h_x^+ = -c_{2\parallel} \mathbf{1} + \begin{bmatrix} -m_{2\parallel} & 0 & 0 & \frac{i}{2}A \\ 0 & m_{2\parallel} & \frac{i}{2}A & 0 \\ 0 & \frac{i}{2}A & -m_{2\parallel} & 0 \\ \frac{i}{2}A & 0 & 0 & m_{2\parallel} \end{bmatrix}, \quad (10)$$

$$h_y = \begin{bmatrix} \xi_+(k_y) & 0 & 0 & -iAk_y a \\ 0 & \xi_-(k_y) & -iAk_y a & 0 \\ 0 & iAk_y a & \xi_+(k_y) & 0 \\ iAk_y a & 0 & 0 & \xi_-(k_y) \end{bmatrix}, \quad (11)$$

$$h_z^+ = -c_{2\perp} \mathbf{1} + \begin{bmatrix} -m_{2\perp} & \frac{i}{2}B & 0 & 0 \\ \frac{i}{2}B & m_{2\perp} & 0 & 0 \\ 0 & 0 & -m_{2\perp} & -\frac{i}{2}B \\ 0 & 0 & -\frac{i}{2}B & m_{2\perp} \end{bmatrix}, \quad (12)$$

where

$$\tilde{c}_0 = c_0 + 2c_{2\parallel} + 2c_{2\perp}, \quad (13)$$

$$\tilde{m}_0 = m_0 + 2m_{2\parallel} + 2m_{2\perp}, \quad (14)$$

$$\xi_{\pm}(k_y) = (c_{2\parallel} \pm m_{2\parallel}) k_y^2 a^2. \quad (15)$$

Note that the Wilson mass term $M_{\mathbf{k}}$ in the original continuum model is now modified to

$$M_{\mathbf{k}}^{\text{dis}} = m_0 + m_{2\parallel} \{ 2[1 - \cos(k_x a)] + (k_y a)^2 \} + m_{2\perp} 2[1 - \cos(k_z a)]. \quad (16)$$

We focus on the weak topological phase with $\boldsymbol{\nu} \equiv (0, 0, 1)$ stabilized when the parameters satisfy¹¹⁾

$$m_{2\parallel} > \frac{1}{4}|m_0| > m_{2\perp} > \frac{1}{4}|m_0| - m_{2\parallel}, \quad (17)$$

where $m_0 < 0$ and $m_{2\parallel} > |c_{2\parallel}| \geq 0$ are assumed. This condition fixes the sign of the mass term at four symmetric points on the $k_x k_z$ -plane with $k_y = 0$ as follows:

$$M_{\mathbf{k}}^{\text{dis}} = \begin{cases} m_0 < 0, & \mathbf{k}' = (0, 0) \\ m_0 + 4m_{2\parallel} > 0, & \mathbf{k}' = (\pi/a, 0) \\ m_0 + 4m_{2\perp} < 0, & \mathbf{k}' = (0, \pi/a) \\ m_0 + 4m_{2\parallel} + 4m_{2\perp} > 0, & \mathbf{k}' = (\pi/a, \pi/a) \end{cases}, \quad (18)$$

where $\mathbf{k}' = (k_x, k_z)$. This indicates that, on the side surface in the yz -plane, the Dirac point appears at $(k_y, k_z) = (0, 0)$ and $(0, \pi/a)$.

Let us find two basis functions for low-energy states localized near the surface by solving the eigenvalue equation for the x -direction with j fixed. We show below that

the resulting basis functions describe the 1D helical channel arising from the j th QSH layer. The procedure is similar to that of Ref. 22 developed on the basis of earlier works.^{21,23,24} The eigenvalue equation now of concern is written as

$$H_x|\psi(j)\rangle = E_\perp|\psi(j)\rangle \quad (19)$$

for a given j , where

$$|\psi(j)\rangle = \sum_{i=1}^{\infty} |i, j\rangle \psi(i). \quad (20)$$

Since its solutions localized near the surface are necessary for our argument, the appropriate boundary condition for $\psi(i)$ is $\psi(0) = \psi(\infty) = {}^t(0, 0, 0, 0)$. Solving Eq. (19) under the required boundary condition, we obtain two degenerate solutions $|\psi_+(j)\rangle$ and $|\psi_-(j)\rangle$ with

$$E_\perp = \tilde{c}_0 - \frac{c_{2\parallel}}{m_{2\parallel}} \tilde{m}_0, \quad (21)$$

where the detailed derivation is given in the Appendix. The resulting expression of $|\psi_\pm(j)\rangle$ is given as

$$|\psi_\pm(j)\rangle = |\psi_0(j)\rangle \mathbf{v}_\pm \quad (22)$$

with

$$\mathbf{v}_+ = \frac{1}{\sqrt{2}} \begin{bmatrix} 0 \\ -i\sqrt{1 + \frac{c_{2\parallel}}{m_{2\parallel}}} \\ \sqrt{1 - \frac{c_{2\parallel}}{m_{2\parallel}}} \\ 0 \end{bmatrix}, \quad (23)$$

$$\mathbf{v}_- = \frac{1}{\sqrt{2}} \begin{bmatrix} \sqrt{1 - \frac{c_{2\parallel}}{m_{2\parallel}}} \\ 0 \\ 0 \\ -i\sqrt{1 + \frac{c_{2\parallel}}{m_{2\parallel}}} \end{bmatrix}, \quad (24)$$

and

$$|\psi_0(j)\rangle = \mathcal{C} \sum_{i=1}^{\infty} (\rho_+^i - \rho_-^i) |i, j\rangle, \quad (25)$$

where \mathcal{C} is a normalization constant, and ρ_+ and ρ_- are constants given by Eq. (A.16) satisfying $|\rho_\pm| < 1$. Note that $|\psi_+(j)\rangle$ and $|\psi_-(j)\rangle$ play the role of the basis functions for low-energy surface states. Clearly, $|\psi_0(j)\rangle$ represents the penetration of surface states into the bulk.

In terms of the basis functions presented above, we can express a low-energy surface state as

$$|\Psi\rangle = \sum_{j=1}^M (\alpha_j |\psi_+(j)\rangle + \beta_j |\psi_-(j)\rangle). \quad (26)$$

We derive an effective Hamiltonian for α_j and β_j in the following.²¹ For this state, the eigenvalue equation is written as

$$(H_y + H_z) |\Psi\rangle = (E - E_\perp) |\Psi\rangle. \quad (27)$$

Taking the inner product of both sides of Eq. (27) with $\mathbf{v}_+^\dagger \langle \psi_0(j)|$ and $\mathbf{v}_-^\dagger \langle \psi_0(j)|$, we obtain a set of equations for α_j and β_j :

$$\begin{aligned} & \gamma A(k_y a) \alpha_j + t \alpha_{j-1} + t \alpha_{j+1} \\ & - \frac{\gamma}{2} B \beta_{j-1} + \frac{\gamma}{2} B \beta_{j+1} = (E - E_\perp) \alpha_j, \end{aligned} \quad (28)$$

$$\begin{aligned} & -\gamma A(k_y a) \beta_j + t \beta_{j-1} + t \beta_{j+1} \\ & + \frac{\gamma}{2} B \alpha_{j-1} - \frac{\gamma}{2} B \alpha_{j+1} = (E - E_\perp) \beta_j, \end{aligned} \quad (29)$$

where

$$\gamma = \sqrt{1 - \left(\frac{c_{2\parallel}}{m_{2\parallel}} \right)^2}, \quad (30)$$

$$t = -c_{2\perp} + \frac{c_{2\parallel}}{m_{2\parallel}} m_{2\perp}. \quad (31)$$

Let us rewrite the basis functions as $|\psi_+(j)\rangle \rightarrow |j\rangle_\uparrow$ and $|\psi_-(j)\rangle \rightarrow |j\rangle_\downarrow$, erasing the degree of freedom with respect to the x -direction, and express an arbitrary wave function as

$$|\Psi\rangle = \sum_{j=1}^M |j\rangle \begin{bmatrix} \alpha_j \\ \beta_j \end{bmatrix} \quad (32)$$

with $|j\rangle \equiv \{|j\rangle_\uparrow, |j\rangle_\downarrow\}$. Then, the effective 2D Hamiltonian is given by

$$\begin{aligned} H_{2D} = & \sum_{j=1}^M |j\rangle \begin{bmatrix} E_\perp + \gamma A k_y a & 0 \\ 0 & E_\perp - \gamma A k_y a \end{bmatrix} \langle j| \\ & + \sum_{j=1}^{M-1} \left\{ |j+1\rangle \begin{bmatrix} t & -\frac{\gamma}{2} B \\ \frac{\gamma}{2} B & t \end{bmatrix} \langle j| + \text{h.c.} \right\}. \end{aligned} \quad (33)$$

We can show that $H_{2D}|\Psi\rangle = E|\Psi\rangle$ is equivalent to Eqs. (28) and (29). Clearly, $|j\rangle_\uparrow$ and $|j\rangle_\downarrow$ respectively represent the right-going and left-going branches of the edge helical channel arising from the j th QSH layer. This indicates that the derived model is equivalent to a series of 1D helical channels, each of which is coupled with its nearest neighbors. The expression of H_{2D} with Eqs. (21), (30), and (31) is the central result of this paper.

3. Analytical Treatment of the 2D Model

Let us briefly consider the effective 2D Hamiltonian given in Eq. (33) in an analytical manner. If the periodic boundary condition is artificially imposed in the z -direction and the limit of $M \rightarrow \infty$ is taken, the dispersion relation is given by

$$E = E_\perp + 2t \cos k_z a \pm \gamma \sqrt{(A k_y a)^2 + (B \sin k_z a)^2}. \quad (34)$$

This indicates that two Dirac cones centered at $(k_y, k_z) = (0, 0)$ and $(0, \pi/a)$ appear in the reciprocal space.¹¹ This is a characteristic feature of WTIs. The Dirac point energies E_0 at $(0, 0)$ and E_π at $(0, \pi/a)$ are respectively

expressed as

$$\begin{aligned} E_0 &= E_\perp + 2t \\ &= c_0 + 2c_{2\parallel} - \frac{c_{2\parallel}}{m_{2\parallel}} (m_0 + 2m_{2\parallel}), \end{aligned} \quad (35)$$

$$\begin{aligned} E_\pi &= E_\perp - 2t \\ &= c_0 + 2c_{2\parallel} + 4c_{2\perp} - \frac{c_{2\parallel}}{m_{2\parallel}} (m_0 + 2m_{2\parallel} + 4m_{2\perp}). \end{aligned} \quad (36)$$

Turning to the realistic case in which Dirac electrons are confined in the finite region of $M \geq j \geq 1$, we construct eigenstates at an energy ϵ . In this case, a subband structure should appear reflecting the confinement of Dirac electrons. It is worth mentioning that Dirac electrons cannot be confined if only one Dirac cone exists in the reciprocal space. The presence of two Dirac cones enables the confinement as we see below. For simplicity, we restrict our consideration to the case of $t = 0$. Let us assume that eigenfunctions are expressed in the form of

$$\begin{bmatrix} \alpha_j \\ \beta_j \end{bmatrix} = \chi(j) \begin{bmatrix} a \\ b \end{bmatrix}, \quad (37)$$

where the transverse function $\chi(j)$ must satisfy the boundary condition of $\chi(0) = \chi(M+1) = 0$. We can construct $\chi(j)$ that satisfies this condition by superposing two wave functions of different Dirac cones¹¹⁾ sharing an identical eigenvector. As a result, we find that

$$\begin{aligned} \chi_m(j) &\propto \left(e^{iq_m z_j} - e^{i\left(\frac{\pi}{a} - q_m\right)z_j} \right) \\ &\propto \left(e^{iq_m z_j} - (-1)^j e^{-iq_m z_j} \right), \end{aligned} \quad (38)$$

where $z_j = ja$ and $q_m = m\pi/[(M+1)a]$ with

$$m = \pm\frac{1}{2}, \pm\frac{3}{2}, \dots, \pm\frac{M-1}{2} \quad (39)$$

for an even M , and

$$m = 0, \pm 1, \pm 2, \dots, \pm\frac{M-1}{2} \quad (40)$$

for an odd M . The dispersion relation for the m th subband is given by

$$E_m(k_y) = E_\perp \pm \sqrt{(\gamma A k_y a)^2 + \Delta_m^2} \quad (41)$$

with

$$\Delta_m = \gamma B \sin q_m a. \quad (42)$$

The corresponding eigenvector is expressed as

$$\begin{bmatrix} a_m \\ b_m \end{bmatrix} \propto \begin{bmatrix} -i\Delta_m \\ E_\perp + \gamma A k_y a - E_m(k_y) \end{bmatrix}. \quad (43)$$

Each subband with $m \neq 0$ is doubly degenerate since $|\Delta_m| = |\Delta_{-m}|$. We see in the next section that this degeneracy is lifted when $t \neq 0$.

The parity effect can be observed in Eq. (41). For an

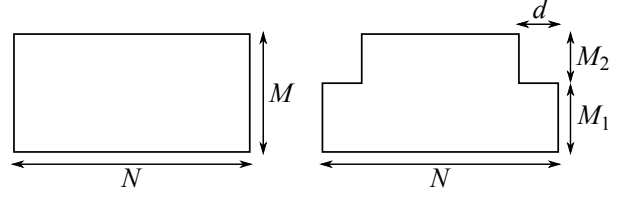


Fig. 2. Cross sections of prism-shaped systems considered in the text: rectangular cross section (left) and cross section with an atomic step of depth d on both side surfaces (right).

odd M , we see that Δ_m vanishes for $m = 0$, indicating that the system has a gapless excitation spectrum. Contrastingly, $m = 0$ is not allowed for an even M as indicated in Eq. (39), so the finite-size gap $2\Delta_{\frac{1}{2}}$ opens across the Dirac point at which $E = E_\perp$. Here, it is meaningful to point out a peculiar property of the zero-energy mode with $m = 0$. Note that $\chi_0(j)$ given above has a finite amplitude only at sites with an odd j and vanishes otherwise. Thus, even though disorder is introduced in B , this mode remains an eigenfunction of H_{2D} with $\Delta_0 = 0$ although the corresponding vector ${}^t[a, b]$ in Eq. (37) is no longer j -independent. In this sense, the zero-energy mode is robust against disorder.

4. Comparison between the 2D and 3D Models

In this section, we numerically obtain an excitation spectrum (i.e., subband structure) of Dirac electrons on a side surface of height M on the basis of the effective 2D Hamiltonian H_{2D} . By comparing the resulting subband structure with that obtained from the 3D bulk Hamiltonian H_{3D} , we examine the validity of our effective model. In determining the subband structure on the basis of H_{3D} , we consider an infinitely long rectangular prism-shaped system of height M and width N (i.e., $N \geq i \geq 1$). Its cross section is shown in the left panel of Fig. 2. This system has the two side surfaces, on which low-energy states appear. We expect that, if N is chosen to be sufficiently large, the low-energy states on one surface and those on the other surface are exactly degenerate without mutual coupling, and that both of them are comparable to those described by H_{2D} . Note that H_{3D} provides us with not only the subband structure of surface states but also the band structure of bulk states. Setting $N = 20$, we perform numerical calculations for the two cases of $t/A = 0$ and $t/A = 0.02$ to observe the effect of t . The parameters are fixed except for $c_{2\perp}$ as follows: $B/A = 0.4$, $m_0/A = -0.5$, $m_{2\parallel}/A = 0.5$, $m_{2\perp}/A = -0.1$, $c_0/A = -1.0$, and $c_{2\parallel}/A = 0.02$. The value of $c_{2\perp}$ is chosen as $c_{2\perp}/A = -0.004$ in the case of $t/A = 0$ and $c_{2\perp}/A = -0.024$ in the case of $t/A = 0.02$. We find that $E_\perp/A = -0.98$ in the case of $t/A = 0$ and $E_\perp/A = -1.02$ in the case of $t/A = 0.02$.

Figure 3 shows the band structure in the case of $t/A = 0$ for $M = 5$ and 6, where dashed (red) lines and

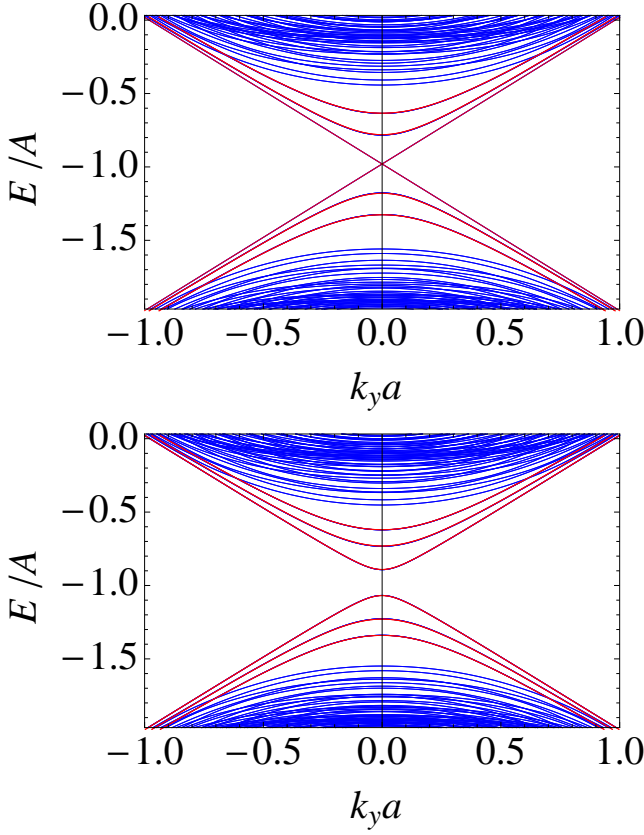


Fig. 3. (Color online) Band structures in the case of $t/A = 0$ for $M = 5$ (upper panel) and $M = 6$ (lower panel), where dashed (red) lines and solid (blue) lines respectively represent the results obtained from the effective 2D model and 3D model.

solid (blue) lines respectively represent the results obtained from H_{2D} and H_{3D} . In the subband structure of surface states inside the bulk gap, the solid (blue) lines completely overlap the dashed (red) ones. This means that the result of the effective 2D model is identical to that of the 3D model concerning the surface states. As noted in the previous section, each subband of surface states is doubly degenerate except for the one with a linear dispersion. The band structure of bulk states consists of only solid (blue) lines obtained from H_{3D} since H_{2D} can describe only surface states. Figure 4 shows the band structure in the case of $t/A = 0.02$ for $M = 5$ and 6. Again, the solid (blue) lines completely overlap the dashed (red) ones for surface states, indicating that the result of the effective 2D model is identical to that of the 3D model. In this case, the degeneracy of each subband of surface states is slightly lifted due to the nonzero t .

In the remainder of this section, we examine the applicability of the effective 2D model to the situation where a side surface contains an atomic step. As an example, let us consider a prism-shaped system with the cross section shown in the right panel of Fig. 2, where both side surfaces of the M layers ($M \equiv M_1 + M_2$) contain an

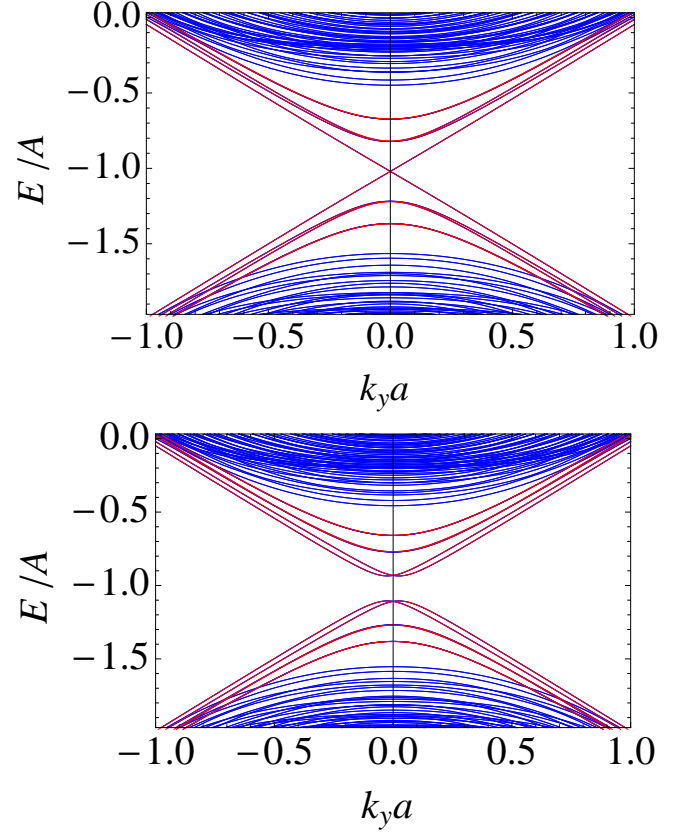


Fig. 4. (Color online) Band structures in the case of $t/A = 0.02$ for $M = 5$ (upper panel) and $M = 6$ (lower panel), where dashed (red) lines and solid (blue) lines respectively represent the results obtained from the effective 2D model and 3D model.

atomic step of depth d . We assume that the left and right atomic steps are located between the M_1 th layer and the $M_1 + 1$ th layer, separating the system into subsystems of M_1 and M_2 layers. Both the side surfaces have an identical subband structure, which is determined by H_{3D} . Our purpose is to answer the question of whether the subband structure can be reproduced on the basis of H_{2D} . The most important effect of an atomic step upon surface electrons is that it reduces electron hopping between neighboring helical channels across it. Thus, we expect to be able to describe the subband structure in terms of H_{2D} by reducing the corresponding hopping terms. According to this observation, we propose the use of the following Hamiltonian:

$$\begin{aligned} \tilde{H}_{2D} = & \sum_{j=1}^M |j\rangle \begin{bmatrix} E_{\perp} + \gamma A k_y a & 0 \\ 0 & E_{\perp} - \gamma A k_y a \end{bmatrix} \langle j| \\ & + \sum_{j=1}^{M-1} \eta_j \left\{ |j+1\rangle \begin{bmatrix} t & -\frac{\gamma}{2} B \\ \frac{\gamma}{2} B & t \end{bmatrix} \langle j| + \text{h.c.} \right\}, \quad (44) \end{aligned}$$

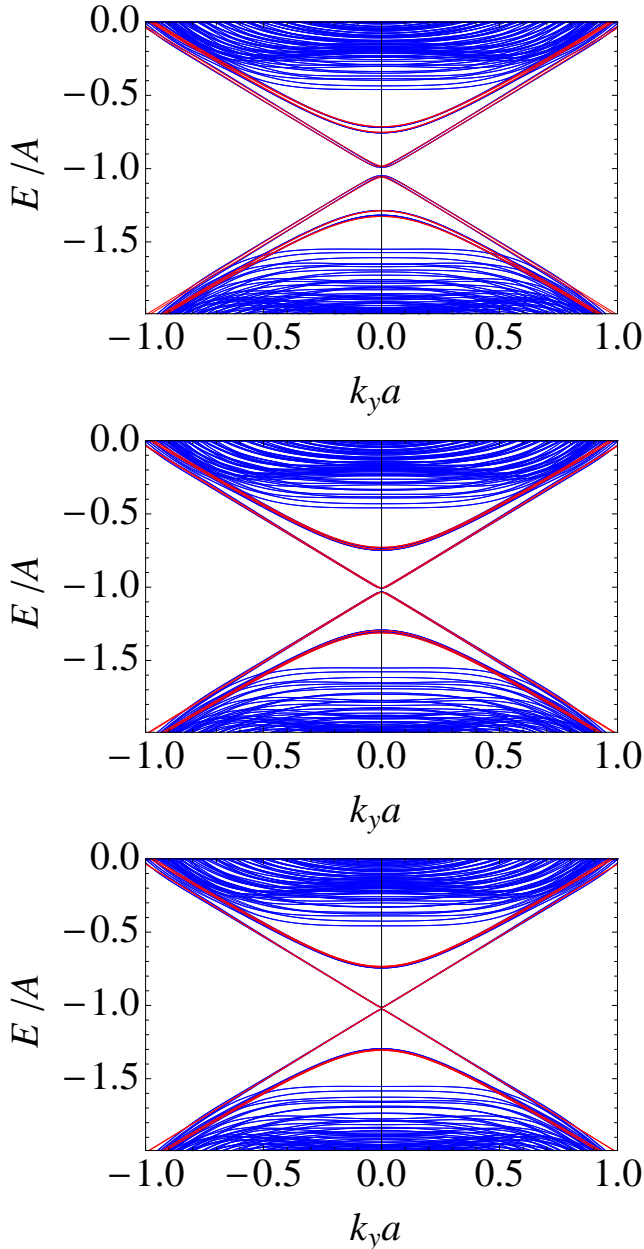


Fig. 5. (Color online) Band structures in the case of $M_1 = M_2 = 3$ for $d = 1$ (upper panel), $d = 2$ (middle panel), and $d = 3$ (lower panel), where dashed (red) lines and solid (blue) lines respectively represent the results obtained from the effective 2D model and 3D model.

where

$$\eta_j = \begin{cases} \delta & (j = M_1) \\ 1 & (j \neq M_1) \end{cases} \quad (45)$$

with $\delta < 1$. As δ represents the overlap between the basis functions for the M_1 th and $M_1 + 1$ th helical channels, we expect from Eq. (25) that it decreases roughly exponentially with increasing d . Treating δ as a fitting parameter, we try to reproduce the subband structure using \tilde{H}_{2D} .

Figure 5 shows the band structure in the case of $M_1 = M_2 = 3$ with step depths $d = 1, 2$, and 3 from top to bottom, where dashed (red) lines and solid (blue) lines respectively represent the results obtained from \tilde{H}_{2D} and H_{3D} . The set of parameters in the case of $t/A = 0.02$ is employed, and the best fitting is found at $\delta = 0.375, 0.15$, and 0.05 , respectively, for $d = 1, 2$, and 3 . In Fig. 5, the solid (blue) lines again completely overlap the dashed (red) ones in the subband structure of surface states inside the bulk gap. This means that \tilde{H}_{2D} accurately reproduces the subband structure even in the presence of an atomic step.

As long as we focus on surface states, the system under consideration can be regarded as two coupled side surfaces consisting of three layers. It is clearly equivalent to a six-layer side surface at $d = 0$, and it approaches two decoupled side surfaces with increasing d . We find from Fig. 5 that the lowest subband shows a nearly linear dispersion, which is a characteristic feature of odd-layer systems. We also find that the lowest subband reveals a finite-size gap that very rapidly decreases with increasing d . Obviously, the presence of a finite-size gap is a characteristic feature of even-layer systems. This implies that the subband structure of surface states in the presence of an atomic step reflects not only the parity of M_1 and M_2 but also that of $M_1 + M_2$ when d is sufficiently small.

5. Summary

In this paper, we have derived an effective 2D model for Dirac electrons on a side surface of weak topological insulators starting from the 3D Wilson-Dirac Hamiltonian for bulk topological insulators. Although the resulting 2D model itself is similar to those proposed in Refs. 14 and 15, our approach has an advantage that all the parameters in the 2D model are directly connected with those in the original 3D model. It is shown that the 2D model accurately reproduces the spectrum of surface Dirac electrons determined by the 3D model, indicating its validity. It is also shown that the model is applicable to a side surface with an atomic step. Although only the case with a single step is treated there, the extension to a case with multiple steps is straightforward.

Acknowledgment

The authors thank K.-I. Imura and Y. Yoshimura for valuable discussions. This work was supported by a Grant-in-Aid for Scientific Research (C) (No. 24540375).

Appendix

Let us find two wave functions $\psi(j)$ with which $|\psi(j)\rangle$ satisfies the eigenvalue equation (19). Considering the matrix form of h_x^+ , we find that one of them is in the form of $\psi(j) = {}^t(v_1, 0, 0, v_2)$ and the other is $\psi(j) = {}^t(0, v_2, v_1, 0)$. Below, we mainly treat the first type, $\psi(j) = {}^t(v_1, 0, 0, v_2)$, as the second type can be obtained by rearranging the elements of the first type.

Let us find elementary solutions $\phi(i)$ of the eigenvalue equation (19) assuming $\phi(i) = \rho^i \mathbf{v}$ with $\mathbf{v} = {}^t(v_1, 0, 0, v_2)$. Under this assumption, the eigenvalue equation is reduced to

$$\begin{bmatrix} \epsilon(\rho) + M(\rho) & A(\rho) \\ A(\rho) & \epsilon(\rho) - M(\rho) \end{bmatrix} \mathbf{v}' = E_{\perp} \mathbf{v}', \quad (\text{A}\cdot 1)$$

where $\mathbf{v}' = {}^t(v_1, v_2)$ and

$$\epsilon(\rho) = \tilde{c}_0 - c_{2\parallel} (\rho + \rho^{-1}), \quad (\text{A}\cdot 2)$$

$$M(\rho) = \tilde{m}_0 - m_{2\parallel} (\rho + \rho^{-1}), \quad (\text{A}\cdot 3)$$

$$A(\rho) = -\frac{i}{2} A (\rho - \rho^{-1}). \quad (\text{A}\cdot 4)$$

Equation (A.1) holds only when

$$[\epsilon(\rho) - E_{\perp}]^2 - M(\rho)^2 - A(\rho)^2 = 0. \quad (\text{A}\cdot 5)$$

Let $\phi_{\pm}(i) \equiv \rho_{\pm}^i \mathbf{v}_{\pm}$ be two different elementary solutions of Eq. (19), in terms of which we can express a general solution as

$$\boldsymbol{\psi}(i) = d_+ \rho_+^i \mathbf{v}_+ + d_- \rho_-^i \mathbf{v}_-. \quad (\text{A}\cdot 6)$$

The boundary condition of $\boldsymbol{\psi}(\infty) = {}^t(0, 0, 0, 0)$ requires

$$|\rho_{\pm}| < 1. \quad (\text{A}\cdot 7)$$

The other boundary condition of $\boldsymbol{\psi}(0) = {}^t(0, 0, 0, 0)$ requires

$$\mathbf{v}_+ = \mathbf{v}_- \quad (\text{A}\cdot 8)$$

for $\rho_+ \neq \rho_-$ with $d_- = -d_+$.

Now we consider the case when $\mathbf{v}_+ = \mathbf{v}_-$ (or equivalently $\mathbf{v}'_+ = \mathbf{v}'_-$) holds. It is instructive to rewrite Eq. (A.1) as

$$\begin{bmatrix} \frac{\epsilon(\rho_{\pm}) + M(\rho_{\pm}) - E_{\perp}}{A(\rho_{\pm})} & 1 \\ 1 & \frac{\epsilon(\rho_{\pm}) - M(\rho_{\pm}) - E_{\perp}}{A(\rho_{\pm})} \end{bmatrix} \mathbf{v}'_{\pm} = \mathbf{0}. \quad (\text{A}\cdot 9)$$

This indicates that $\mathbf{v}'_+ = \mathbf{v}'_-$ is realized for $\rho_+ \neq \rho_-$ only when

$$\frac{\epsilon(\rho_+) + M(\rho_+) - E_{\perp}}{A(\rho_+)} = \frac{\epsilon(\rho_-) + M(\rho_-) - E_{\perp}}{A(\rho_-)} \quad (\text{A}\cdot 10)$$

and

$$\frac{\epsilon(\rho_+) - M(\rho_+) - E_{\perp}}{A(\rho_+)} = \frac{\epsilon(\rho_-) - M(\rho_-) - E_{\perp}}{A(\rho_-)} \quad (\text{A}\cdot 11)$$

simultaneously hold.²²⁾ These equations require that $M(\rho_{\pm}) \propto \epsilon(\rho_{\pm}) - E_{\perp}$. This relation determines E_{\perp} as

$$E_{\perp} = \tilde{c}_0 - \frac{c_{2\parallel}}{m_{2\parallel}} \tilde{m}_0, \quad (\text{A}\cdot 12)$$

which can be rewritten as

$$\epsilon(\rho_{\pm}) - E_{\perp} = \frac{c_{2\parallel}}{m_{2\parallel}} M(\rho_{\pm}). \quad (\text{A}\cdot 13)$$

Combining Eqs. (A.5) and (A.13), we find that

$$\gamma M(\rho_{\pm}) = \pm i A(\rho_{\pm}) \quad (\text{A}\cdot 14)$$

with

$$\gamma = \sqrt{1 - \left(\frac{c_{2\parallel}}{m_{2\parallel}} \right)^2}. \quad (\text{A}\cdot 15)$$

As shown later, solutions with $|\rho_{\pm}| < 1$ are always obtained in the case of $\gamma M(\rho_{\pm}) = i A(\rho_{\pm})$ under the condition of Eq. (17) with $A > 0$. This immediately yields

$$\rho_{\pm} = \frac{\gamma \tilde{m}_0 \pm \sqrt{(\gamma \tilde{m}_0)^2 - 4(\gamma m_{2\parallel})^2 + A^2}}{2(\gamma m_{2\parallel} + \frac{A}{2})} \quad (\text{A}\cdot 16)$$

and

$$\mathbf{v}' = \frac{1}{\sqrt{2}} \begin{bmatrix} \sqrt{1 - \frac{c_{2\parallel}}{m_{2\parallel}}} \\ -i \sqrt{1 + \frac{c_{2\parallel}}{m_{2\parallel}}} \end{bmatrix}, \quad (\text{A}\cdot 17)$$

where $\mathbf{v}' \equiv \mathbf{v}'_+ = \mathbf{v}'_-$. Now we can express the wave function $\boldsymbol{\psi}_-(i)$ of the first type as

$$\boldsymbol{\psi}_-(i) = \mathcal{C} (\rho_+^i - \rho_-^i) \mathbf{v}_- \quad (\text{A}\cdot 18)$$

with

$$\mathbf{v}_- = \frac{1}{\sqrt{2}} \begin{bmatrix} \sqrt{1 - \frac{c_{2\parallel}}{m_{2\parallel}}} \\ 0 \\ 0 \\ -i \sqrt{1 + \frac{c_{2\parallel}}{m_{2\parallel}}} \end{bmatrix}, \quad (\text{A}\cdot 19)$$

where \mathcal{C} is a constant to be determined by the normalization condition of $\sum_{i=1}^{\infty} |\mathcal{C} (\rho_+^i - \rho_-^i)|^2 = 1$. The wave function $\boldsymbol{\psi}_+(i)$ of the second type is expressed by replacing \mathbf{v}_- with \mathbf{v}_+ given by

$$\mathbf{v}_+ = \frac{1}{\sqrt{2}} \begin{bmatrix} 0 \\ -i \sqrt{1 + \frac{c_{2\parallel}}{m_{2\parallel}}} \\ \sqrt{1 - \frac{c_{2\parallel}}{m_{2\parallel}}} \\ 0 \end{bmatrix}. \quad (\text{A}\cdot 20)$$

Substituting $\boldsymbol{\psi}_{\pm}(i)$ into Eq. (20), we obtain $|\psi_{\pm}(j)\rangle$ given in Eq. (22)

Now we turn to Eq. (A.14) and show that solutions with $|\rho_{\pm}| < 1$ are obtained only in the case of $\gamma M(\rho_{\pm}) = i A(\rho_{\pm})$ under the condition of Eq. (17) if $A > 0$ is assumed without loss of generality. To do so, let us examine the two cases of $\gamma M(\rho_{\pm}) = i A(\rho_{\pm})$ and $\gamma M(\rho_{\pm}) = -i A(\rho_{\pm})$. In the first case, ρ_{\pm} is obtained as

$$\rho_{1\pm} = \frac{\gamma \tilde{m}_0 \pm \sqrt{D}}{2(\gamma m_{2\parallel} + \frac{A}{2})}, \quad (\text{A}\cdot 21)$$

while

$$\rho_{2\pm} = \frac{\gamma \tilde{m}_0 \pm \sqrt{D}}{2(\gamma m_{2\parallel} - \frac{A}{2})} \quad (\text{A}\cdot 22)$$

in the second case, where

$$D \equiv (\gamma\tilde{m}_0)^2 - 4(\gamma m_{2\parallel})^2 + A^2. \quad (\text{A}\cdot 23)$$

We show below that $|\rho_{1\pm}| < 1$ always holds while $|\rho_{2\pm}| < 1$ never holds. That is, the appropriate solutions are obtained in the case of $\gamma M(\rho_{\pm}) = iA(\rho_{\pm})$. We separately consider the cases of $D < 0$ and $D > 0$ below. Note that $m_0 < 0$ and $m_{2\parallel} > 0$ are implicitly assumed in Eq. (17).

A.1 The case of $D < 0$

In this case, Eqs. (A·21) and (A·22) are rewritten as

$$\rho_{1\pm} = \frac{\gamma\tilde{m}_0 \pm i\sqrt{-D}}{2(\gamma m_{2\parallel} + \frac{A}{2})} = \rho_{2\pm}^{-1}. \quad (\text{A}\cdot 24)$$

This immediately yields

$$|\rho_{1\pm}| = \frac{|\gamma m_{2\parallel} - \frac{A}{2}|}{|\gamma m_{2\parallel} + \frac{A}{2}|} < 1 < \frac{|\gamma m_{2\parallel} + \frac{A}{2}|}{|\gamma m_{2\parallel} - \frac{A}{2}|} = |\rho_{2\pm}|. \quad (\text{A}\cdot 25)$$

A.2 The case of $D > 0$

In this case, we can show from Eqs. (A·21) and (A·22) that $\rho_{1\pm}\rho_{2\mp} = 1$, and that $|\rho_{2+}| > |\rho_{1+}|$ and $|\rho_{2-}| > |\rho_{1-}|$ since $m_{2\parallel} > 0$ and $A > 0$ are assumed. Let us separately treat the two cases of $\tilde{m}_0 > 0$ and $\tilde{m}_0 < 0$.

If $\tilde{m}_0 > 0$, we find that $|\rho_{2+}| > |\rho_{2-}|$ from Eq. (A·22). The combination of this with $|\rho_{2-}| > |\rho_{1-}|$ yields

$$|\rho_{2+}| > |\rho_{1-}|, \quad (\text{A}\cdot 26)$$

indicating that $|\rho_{2+}| > 1$ since $\rho_{1-}\rho_{2+} = 1$. Thus, we see that $|\rho_{2\pm}| < 1$ never holds. Here, we also find from Eq. (A·21) with $\tilde{m}_0 > 0$ that $\rho_{1+} > |\rho_{1-}|$. The above argument indicates that the solution satisfying the boundary condition can be constructed when

$$1 > \rho_{1+}. \quad (\text{A}\cdot 27)$$

We can show that this always holds under the condition of Eq. (17).

If $\tilde{m}_0 < 0$, we find that $|\rho_{2-}| > |\rho_{2+}|$ from Eq. (A·22). The combination of this with $|\rho_{2+}| > |\rho_{1+}|$ yields

$$|\rho_{2-}| > |\rho_{1+}|, \quad (\text{A}\cdot 28)$$

indicating that $|\rho_{2-}| > 1$ since $\rho_{1+}\rho_{2-} = 1$. Thus, we see that $|\rho_{2\pm}| < 1$ never holds. Here, we also find from Eq. (A·21) with $\tilde{m}_0 < 0$ that $|\rho_{1-}| > |\rho_{1+}|$. The above argument indicates that the solution satisfying the bound-

ary condition can be constructed when

$$1 > |\rho_{1-}|. \quad (\text{A}\cdot 29)$$

We can show that this always holds under the condition of Eq. (17).

-
- 1) L. Fu, C. L. Kane, and E. J. Mele, Phys. Rev. Lett. **98**, 106803 (2007).
 - 2) J. E. Moore and L. Balents, Phys. Rev. B **75**, 121306 (2007).
 - 3) R. Roy, Phys. Rev. B **79**, 195322 (2009).
 - 4) C. L. Kane and E. J. Mele, Phys. Rev. Lett. **95**, 146802 (2005).
 - 5) B. A. Bernevig and S.-C. Zhang, Phys. Rev. Lett. **96**, 106802 (2006).
 - 6) Y. Ran, Y. Zhang, and A. Vishwanath, Nat. Phys. **5**, 298 (2009).
 - 7) K.-I. Imura, Y. Takane, and A. Tanaka, Phys. Rev. B **84**, 195406 (2011).
 - 8) Z. Ringel, Y. E. Kraus, and A. Stern, Phys. Rev. B **86**, 045102 (2012).
 - 9) R. S. K. Mong, J. H. Bardarson, and J. E. Moore, Phys. Rev. Lett. **108**, 076804 (2012).
 - 10) C.-X. Liu, X.-L. Qi, and S.-C. Zhang, Physica E **44**, 906 (2012).
 - 11) K.-I. Imura, M. Okamoto, Y. Yoshimura, Y. Takane, and T. Ohtsuki, Phys. Rev. B **86**, 245436 (2012).
 - 12) Y. Yoshimura, A. Matsumoto, Y. Takane, and K.-I. Imura, Phys. Rev. B **88**, 045408 (2013).
 - 13) K. Kobayashi, T. Ohtsuki, and K.-I. Imura, Phys. Rev. Lett. **110**, 236803 (2013).
 - 14) T. Morimoto and A. Furusaki, Phys. Rev. B **89**, 035117 (2014).
 - 15) H. Obuse, S. Ryu, A. Furusaki, and C. Mudry, Phys. Rev. B **89**, 155315 (2014).
 - 16) Y. Takane, J. Phys. Soc. Jpn. **83**, 103706 (2014).
 - 17) B.-H. Yan, L. Muehler, and C. Felser, Phys. Rev. Lett. **109**, 116406 (2012).
 - 18) B. Rasche, A. Isaeva, M. Ruck, S. Borisenko, V. Zabolotnyy, B. Buchner, K. Koepernik, C. Ortix, M. Richter, and J. van den Brink, Nat. Mater. **12**, 422 (2013).
 - 19) P. Tang, B. Yan, W. Cao, S.-C. Wu, C. Felser, and W. Duan, Phys. Rev. B **89**, 041409 (2014).
 - 20) G. Yang, J. Liu, L. Fu, W. Duan, and C. Liu, Phys. Rev. B **89**, 085312 (2014).
 - 21) C.-X. Liu, X.-L. Qi, H. Zhang, X. Dai, Z. Fang, and S.-C. Zhang, Phys. Rev. B **82**, 045122 (2010).
 - 22) M. Okamoto, Y. Takane, and K.-I. Imura, Phys. Rev. B **89**, 125425 (2014).
 - 23) M. König, H. Buhmann, L. W. Molenkamp, T. Hughes, C.-X. Liu, X.-L. Qi, and S.-C. Zhang, J. Phys. Soc. Jpn. **77**, 031007 (2008).
 - 24) W.-Y. Shan, H.-Z. Lu, and S.-Q. Shen, New J. Phys. **12**, 043048 (2010).